ARCHIVES OF ELECTRICAL ENGINEERING VOL. 75(1), pp. 57–78 (2026)

DOI 10.24425/aee.2026.156802

# Non-Fourier Dual-Phase-Lag thermal models using thermoelectric analogy

MARIA STRĄKOWSKA [1]✉, GILBERT DE MEY [2], BOGUSŁAW WIĘCEK [1]

[1] *Institute of Electronics, Lodz University of Technology*
*116 Żeromskiego Str., 90-924 Lodz, Poland*

[2] *Department of Electronics and Information Systems, University of Gent*
*126 Technologiepark – Zwijnaarde, 9052, Gent, Belgium*

*e-mail: {✉ maria.strakowska/boguslaw.wiecek}@p.lodz.pl, gilbert.demey@ugent.be*

(Received: 31.07.2025, revised: 23.01.2026)

**Abstract:** This research presents the modelling of non-Fourier heat conduction using the Single and Dual-Phase-Lag (SPL/DPL) in the frequency domain. Thermal structures can be modelled using Foster, Cauer networks or their compact equivalents, using the analogy with electrical networks. The key aim of such modelling is to simplify the heat transfer processes of geometrically complex thermal structures composed of layers with different materials. In this paper, we propose the analytical solution of the heat transfer equation for a single-layer thermal object in the frequency domain. It is achieved by the transformation of Kirchhoff–Fourier equations into the multi-cell Cauer network that can be easily solved using the node potentials method. In the case of non-Fourier SPL and DPL models, the thermal conductivity is no longer a real value, but it varies with frequency. As a result, the spatially distributed thermal model can be presented as an electrical network consisting of thermal resistances, capacitances and inductances. It makes it possible to take into account diffusive, wave propagation and mixed conductive heat transfer. Such modelling allows confirming the non-Fourier heat transfer in porous-like materials and biostructures with a better understanding of the physical nature of heat transfer, which is still discussed in the scientific literature.

**Key words:** Cauer network, DPL, non-Fourier heat transfer, thermal ladder model, thermoelectric analogy

## Nomenclature

$q$ – heat flux, $\left(\frac{\mathrm{W}}{\mathrm{m}^2}\right)$
$\omega$ – angular frequency, $\left(\frac{\mathrm{rad}}{\mathrm{s}}\right)$
$k$ – thermal conductivity, $\left(\frac{\mathrm{W}}{\mathrm{m}\cdot\mathrm{K}}\right)$
$\widetilde{k}$ – modified thermal conductivity for DPL model, $\left(\frac{\mathrm{W}}{\mathrm{m}\cdot\mathrm{K}}\right)$
$\tau_q$ – relaxation time constant, (s)
$\tau_T$ – thermal gradient time constant, (s)
$c$ – specific heat, $\left(\frac{\mathrm{J}}{\mathrm{kg}\cdot\mathrm{K}}\right)$
$\rho$ – density, $\left(\frac{\mathrm{kg}}{\mathrm{m}^3}\right)$
$T$ – temperature, (K)
$t$ – time, (s)
$s$ – Laplace operator, (rad/s)
$c_{th}$ – thermal capacity per cubic meter $\left(\frac{\mathrm{J}}{\mathrm{m}^3\mathrm{K}}\right)$
$r_{th\,S}$ – thermal resistance per area unit, $\left(\frac{\mathrm{m}^2\mathrm{K}}{\mathrm{W}}\right)$
$S$ – surface, $(\mathrm{m}^2)$
$x$ – distance, (m)
$\Delta V$ – volume, $(\mathrm{m}^3)$
$h_d$ – heat transfer coefficient at the bottom of the structure, $\left(\frac{\mathrm{W}}{\mathrm{m}^2\mathrm{K}}\right)$
$h_0$ – heat transfer coefficient at the surface, $\left(\frac{\mathrm{W}}{\mathrm{m}^2\mathrm{K}}\right)$
$Y_{th}$ – thermal admittance, $\left(\frac{\mathrm{W}}{\mathrm{K}}\right)$
$Z_{th}$ – thermal impedance, $\left(\frac{\mathrm{K}}{\mathrm{W}}\right)$
$G_{th}$ – thermal conductance, $\left(\frac{\mathrm{W}}{\mathrm{K}}\right)$
$R_{th}$ – thermal resistance, $\left(\frac{\mathrm{K}}{\mathrm{W}}\right)$
$C_{th}$ – thermal capacity, $\left(\frac{\mathrm{J}}{\mathrm{K}}\right)$,
$C_{thT}$ – thermal capacity for DPL models, $\left(\frac{\mathrm{J}}{\mathrm{K}}\right)$
$L_{thq}$ – thermal inductance for DPL models, $\left(\frac{\mathrm{K}\cdot\mathrm{s}}{\mathrm{W}}\right)$
$R_{thT}$ – thermal resistance for DPL model, $\left(\frac{\mathrm{K}}{\mathrm{W}}\right)$
$R_{thq}$ – thermal resistance for DPL model, $\left(\frac{\mathrm{K}}{\mathrm{W}}\right)$
$R_0$ – characteristic resistance for thermal transmission long line, $\left(\frac{\mathrm{K}}{\mathrm{W}}\right)$
$v$ – propagation velocity, $\left(\frac{\mathrm{m}}{\mathrm{s}}\right)$
$\widetilde{T}^{(2)}$ – second derivative of temperature, $\left(\frac{\mathrm{K}}{\mathrm{m}^2}\right)$
$R(\Delta x)$ – reminder in the Taylor expansion, $\left(\frac{\mathrm{K}}{\mathrm{m}^2}\right)$

List of abbreviations:

| | |
|---|---|
| DPL | Dual-Phase Lag heat transfer model |
| SPL | Single-Phase Lag heat transfer model |
| FDM | Finite Difference Method |
| F–K | Fourier – Kirchhoff heat transfer model |

## 1. Introduction

The Dual-Phase Lag (DPL) model is of interest to many researchers [1–13]. However, its practical application poses challenges due to the fact that the phase lag phenomenon is primarily observed at the very beginning of the heat process, during the thermal excitation, and appears mostly in very thin structures [14, 15] and porous materials such as skin tissue [7, 16–23]. The thermal response signal is usually very weak, making it difficult to obtain precise measurements. Due to this, it is difficult to confirm that the model is consistent with real structures. There have been attempts in the literature to confirm the existence of the Dual-Phase Lag phenomenon through experiments [24–26], but most confirmations have been done through simulations [2, 7–10, 22] or using available experimental data [11, 21].

The Fourier–Kirchhoff model assumes that heat is transferred due to the presence of a temperature gradient and that the heat is going through the structure without any delay. In contrast, in the DPL model, there are two additional time constants, which result in a delay in heat transfer through the structure. This seems to make the DPL model more physically accurate than the classical Fourier–Kirchhoff approach. But the physical agreement of the DPL model is also questioned by some researchers [3, 27, 28]. The DPL model incorporates two-time constants $\tau_q$ and $\tau_T$, corresponding to thermal relaxation and thermal diffusion, respectively. Solving heat transfer equations in the frequency domain leads to a novel definition of thermal conductivity, which for the DPL model is a complex value and it varies depending on frequency [23] – Eq. (1).

$$\begin{aligned} q &= -\widetilde{k}\frac{\partial T}{\partial x}, \\ \widetilde{k} &= k\frac{1+j\omega\tau_T}{1+j\omega\tau_q}, \end{aligned} \tag{1}$$

where $k$ is the classical thermal conductivity of a material defined by the Fourier law.

Another issue with the DPL model is that there are no convincing reference values for the mentioned time constants in the literature. In some references, $\tau_q$ is lower than $\tau_T$ [29], in others, opposite [30, 31]. The ratio between these time constants determines the nature of the heat flow, whether it is diffusive or wave-like. From a physical perspective, it is important to consider whether such an approach has a valid physical meaning [3, 28, 32]. In this article, we present a comparison of two consistent models: the first is solved analytically in the frequency domain, and the second is based on thermo-electrical analogy.

The model based on Cauer ladder networks is widely used in various engineering fields, particularly in microelectronics. This approach can simply model multi-layer structures, heat sinks, and materials with complex geometries. In the classical Cauer ladder network, the standard approach uses thermal resistances and thermal capacitances to represent the thermal impedance in a system [33, 34]. Modifications of the Cauer network can also be found, where inductors and/or capacitors are used instead of resistors in the circuit [35–37]. Such circuits are applied to model wireless systems or transformers.

Most thermal models found in the literature are based on the diffusion equation [33–35]. In the case of electronic systems, the so-called compact models are particularly useful and are increasingly popular among researchers and engineers. These models consist of thermal resistors and capacitances related to material properties, and current and voltage sources imitating power and temperature. The main advantage of using compact modeling is the available software package, such as SPICE, which can not only calculate currents and voltages, but also temperatures and heat flows.

As an example, an electrothermal SPICE simulation was performed for the current mirror configuration with four cascades [38]. The same approach is also used for air flow simulation over electronic boards and components. Compact thermal models are made providing a relationship between the temperature of the junction and the external surfaces cooled by the air flow [33, 39–42].

Recently, non-Fourier heat transfer modeling has found applications in biomedicine, as tissue is treated as a type of porous material in which heat not only diffuses but also propagates as a wave. Interesting results show that in cancerous tissue, heat can partially propagate as an acoustic wave [8–11, 43]. There is currently growing interest in porous structures for various thermal management applications. Porous materials are used to transport fluids and phase-change materials, thereby increasing cooling and heat removal efficiency [44, 45].

Our work presents a comparison of analytical models for heat transfer solved in the frequency domain and their equivalent electro-thermal analogy obtained using the Finite Difference Method to solve heat conduction equations. For the Fourier–Kirchhoff heat transfer model, the equivalent electrical solution is the Cauer ladder. For SPL and DPL models, modifications involving thermal impedance or admittance are applied, incorporating different passive elements such as capacitors and inductors, in place of resistors in the $R_{th}$ branch of the Cauer network. Both approaches, the analytical thermal model and the electrical circuit analogy, align well to each other, confirming that in porous-like materials, heat transfer occurs not only by diffusion but also through wave propagation. The problem of the physical behavior of the DPL model can appear when $\tau_q$ is higher than $\tau_T$.

## 2. Finite difference thermal model approximation

1D heat conduction in solids is described by the well-known Fourier–Kirchhoff's (F–K) Formula (2).

$$k\frac{\partial^2 T}{\partial x^2} - c\rho\frac{\partial T}{\partial t} = 0, \tag{2}$$

where $c$ is the specific heat and $\rho$ is the material's density.

The Laplace transform of a derivative is given by (3).

$$\mathcal{L}\left\{\frac{\mathrm{d}T}{\mathrm{d}t}\right\} = sT - T^{+}(0)\,. \tag{3}$$

In this research, we do not need to consider the initial value $T^{+}(0)$. Even though the Laplace variable $s$ is used. We work in the so-called sinusoidal regime. Hence, $s$ can be replaced by $j\omega$ and vice versa. In the sinusoidal regime, well known from the analysis of alternating current electrical networks, the initial condition does not affect the results of interest.

In the frequency domain, after applying the Laplace transformation for $s = j\omega$, Eq. (2) takes the form.

$$k\frac{\mathrm{d}^2 T}{\mathrm{d}x^2} - j\omega c_{th}T = 0, \tag{4}$$

where $c_{th} = c\rho$ denotes the thermal capacity per cubic meter.

Assume that for a small part of the object, heat flows through 3 discrete points at a distance of $2\Delta x$, as shown in Fig. 1.

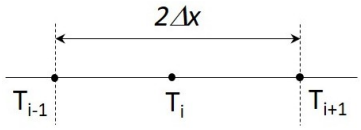


Fig. 1. Discrete thermal object with 3 adjacent points

The Finite Difference Method (FDM) allows approximating the second-order derivative in (4). As a result, the heat transfer equation takes the discrete form.

$$\frac{k\dfrac{T_{i+1}-T_i}{\Delta x} - k\dfrac{T_i - T_{i-1}}{\Delta x}}{\Delta x} - j\omega c_{th}T_i = 0. \tag{5}$$

After introducing the thermal resistance $r_{th\,S}$ per area unit $S$ perpendicular to the heat flux as:

$$r_{th\,S} = \frac{\Delta x}{k}. \tag{6}$$

Equation (5) takes the form:

$$\frac{\dfrac{T_{i+1} - T_i}{r_{th\,S}} - \dfrac{T_i - T_{i-1}}{r_{th\,S}}}{\Delta x} - j\omega c_{th} T_i = 0. \tag{7}$$

Finally, by scaling the last formula by $\Delta V = S\Delta x$, we can obtain the well-known Cauer approximation of the 1D heat flow in the following form.

$$\frac{T_{i+1} - T_i}{R_{th}} + \frac{T_{i-1} - T_i}{R_{th}} - j\omega C_{th} T_i = 0, \tag{8}$$

where:

$$\begin{aligned} R_{th} &= \frac{\Delta x}{kS}, \\ C_{th} &= c\rho S\Delta x. \end{aligned} \tag{9}$$

Using the concept of thermoelectric analogy, Eq. (8) can be presented as an electrical network with 3 nodes, as shown in Fig. 2.

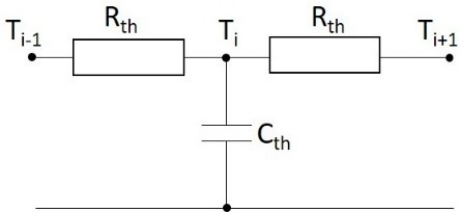


Fig. 2. Thermoelectric analogy circuit of Fourier–Kirchhoff's heat conduction

## 3. DPL extensions

The Dual-Phase-Lag (DPL) extension to heat transfer in solids introduces 2-time constants, one for the heat flux $\tau_q$ and one for the temperature gradient $\tau_T$.

$$q + \tau_q \frac{\partial q}{\partial t} = -k\left(\frac{\partial T}{\partial x} + \tau_T \frac{\partial^2 T}{\partial x \partial t}\right). \tag{10}$$

It is worth to notice that for $\tau_T = \tau_q$, the DPL model returns to the classical Fourier–Kirchhoff's form. Using the Laplace transformation for Eq. (10), it is possible to redefine heat flux and thermal conductivity in more general forms.

$$\begin{aligned} q &= -\widetilde{k}\frac{\partial T}{\partial x}, \\ \widetilde{k} &= k\frac{1 + j\omega\tau_T}{1 + j\omega\tau_q}. \end{aligned} \tag{11}$$

Using the DPL approach, thermal conductivity is a complex value and depends on frequency. In the low-frequency range ($\omega \ll 1/\tau_T$ and $\omega \ll 1/\tau_q$), thermal conductivity reaches the classical value ($\widetilde{k} \to k$), while in the high-frequency range, thermal conductivity may be lower or higher, depending on the ratio of delay times ($\widetilde{k} \to k\tau_T/\tau_q$).

### 3.1. Diffusive heat transfer

Let's assume that $\tau_T > 0$ and $\tau_q = 0$. In this case, the DPL model is reduced to the Single Phase Lag (SPL) form with diffusive heat transfer only. As a result, Eq. (10) can be simplified and takes the form (12).

$$q = -k\left(\frac{\partial T}{\partial x} + \tau_T \frac{\partial^2 T}{\partial x \partial t}\right). \tag{12}$$

Using (12), Eq. (2) can be rewritten as:

$$k\left(\frac{\partial^2 T}{\partial x^2} + \tau_T \frac{\partial^3 T}{\partial x^2 \partial t}\right) - c_{th}\frac{\partial T}{\partial t} = 0. \tag{13}$$

Finally, after the Laplace transformation, we can present the differential equation of heat transfer as

$$k\,(1 + j\omega\tau_T)\,\frac{\mathrm{d}^2 T}{\mathrm{d}x^2} - j\omega c_{th} T = 0. \tag{14}$$

Assuming that thermal conductivity is no longer a real value and depends on frequency, it is worth introducing thermal admittance $Y_{th}$. It consists of a real part – thermal conductivity $G_{th}$ and an imaginary part expressed by thermal capacity $C_{th}$ as in the Eq. (15). The value of thermal conductance $G_{th} = 1/R_{th}$, where $R_{th}$ is given by the Eq. (9).

$$\widetilde{k} = k\,(1 + j\omega\tau_T)\,,$$
$$Y_{th} = \frac{kS}{\Delta x}\,(1 + j\omega\tau_T) = G_{th} + j\omega C_{thT}, \tag{15}$$

where

$$G_{th} = \frac{kS}{\Delta x}, \quad C_{thT} = \tau_T \frac{kS}{\Delta x} = \tau_T G_{th}. \tag{16}$$

As a result, 3-node thermal-electrical analogy networks can be represented as in Fig. 3.

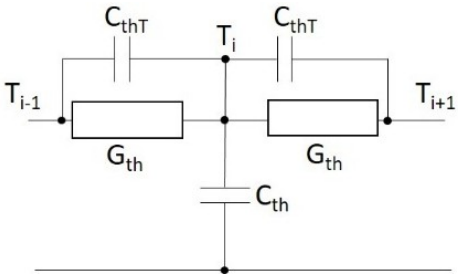


Fig. 3. Thermoelectric analogy circuit of SPL heat conduction for $\tau_q = 0$

### 3.2. Wave propagation heat transfer

Let's assume that $\tau_q > 0$ and $\tau_T = 0$. In this case, the DPL model is reduced to the SPL form with wave propagation character of heat transfer, and Eq. (10) can be simplified to the form:

$$q + \tau_q \frac{\partial q}{\partial t} = -k \frac{\partial T}{\partial x}. \tag{17}$$

As a result, Eq. (2) can be rewritten as:

$$k \frac{\partial^2 T}{\partial x^2} - c_{th} \left( \frac{\partial T}{\partial t} + \tau_q \frac{\partial^2 T}{\partial t^2} \right) = 0. \tag{18}$$

It is worth noting that due to the second derivative of temperature with respect to time, Eq. (18) no longer describes heat diffusion, but wave propagation.

After the Laplace transformation, the differential equation of heat conduction (18) takes the form:

$$\frac{k}{1 + j\omega\tau_q} \frac{\mathrm{d}^2 T}{\mathrm{d}x^2} - j\omega c_{th} T = 0. \tag{19}$$

Assuming that thermal conductivity is no more a real value and it depends on frequency, it is now worth introducing the thermal impedance $Z_{th}$ containing thermal resistance $R_{th}$ and thermal inductance $L_{thq}$ as in Eq. (20).

$$\widetilde{k} = \frac{k}{1 + j\omega\tau_q},$$
$$Z_{th} = \frac{\Delta x}{kS} \left(1 + j\omega\tau_q\right) = R_{th} + j\omega L_{thq}, \tag{20}$$

where:

$$L_{thq} = \tau_q \frac{\Delta x}{kS} = \tau_q R_{th}. \tag{21}$$

Now, the corresponding electrical network consists of 3 components: $R_{th}$, $L_{thq}$ and $C_{th}$ – Fig. 4.

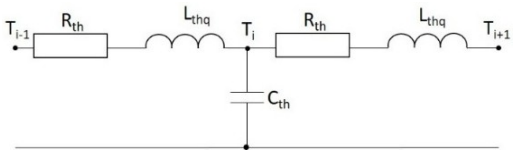


Fig. 4. Thermoelectric analogy circuit of SPL heat conduction for $\tau_T = 0$

### 3.3. Mixed diffusion-wave heat transfer

Let's consider 2 more cases, where both $\tau_T \neq 0$ and $\tau_q \neq 0$ and they are positive. The first case refers to $\tau_T > \tau_q$ It denotes that the diffusive heat flow dominates over the wave nature of thermal energy transfer.

In this case thermal conductivity $\widetilde{k}$ takes the form:

$$\widetilde{k} = k\left(1 + \frac{j\omega\Delta\tau}{1 + j\omega\tau_q}\right), \tag{22}$$

where: $\Delta\tau = \tau_T - \tau_q$.

Equation (15) can be modified to the form:

$$Y_{th} = \frac{kS}{\Delta x}\left(1 + \frac{1}{\dfrac{1}{j\omega\Delta\tau} + \dfrac{\tau_q}{\Delta\tau}}\right). \tag{23}$$

Schematically, Eq. (23) can be presented as the $R_{th}C_{th}$ network as in Fig. 5.

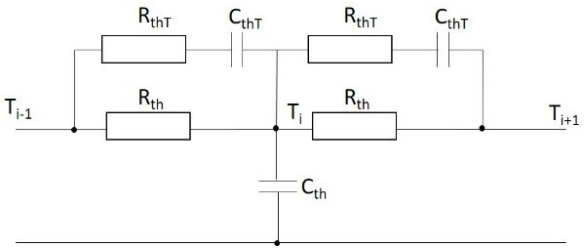


Fig. 5. Thermoelectric analogy circuit of DPL heat conduction for $\tau_T > \tau_q$

The new elements $Z_{thT}$ and $C_{thT}$ are defined as:

$$\begin{aligned} R_{thT} &= \frac{\tau_q}{\Delta\tau}\frac{\Delta x}{kS} = \frac{\tau_q}{\Delta\tau}R_{th}, \\ C_{thT} &= \Delta\tau\frac{kS}{\Delta x} = \Delta\tau G_{th}. \end{aligned} \tag{24}$$

Similarly, in the case of $\tau_q > \tau_T$ wave propagation dominates over diffusion during heat flow in the considered material. In this case, thermal conductivity takes the form (25).

$$\widetilde{k} = k\left(\frac{1 + j\omega\tau_T}{1 + j\omega\left(\tau_T + \Delta\tau\right)}\right), \tag{25}$$

where $\Delta\tau = \tau_q - \tau_T$.

Equation (20) can be modified to the form (26).

$$Z_{th} = \frac{\Delta x}{kS}\left(1 + \frac{1}{\dfrac{1}{j\omega\Delta\tau} + \dfrac{\tau_T}{\Delta\tau}}\right). \tag{26}$$

The new elements $R_{thq}$ and $L_{thq}$ are defined by (27).

$$\begin{aligned} R_{thq} &= \frac{\Delta\tau}{\tau_t}\frac{\Delta x}{kS} = \frac{\Delta\tau}{\tau_q}R_{th}, \\ L_{thq} &= \Delta\tau\frac{\Delta x}{kS} = \Delta\tau R_{th}. \end{aligned} \tag{27}$$

Schematically, Eq. (26) can be presented as the $R_{th}L_{th}C_{th}$ network as in Fig. 6.

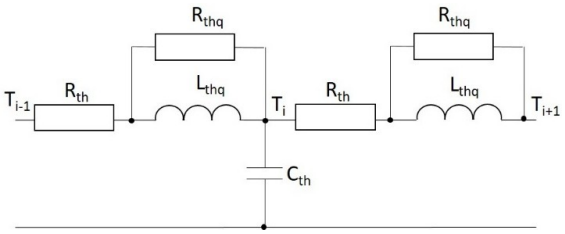


Fig. 6. Thermoelectric analogy circuit of DPL heat conduction for $\tau_q > \tau_T$

## 4. Analytical DPL thermal model in the frequency domain

In order to validate the discrete $R_{th}L_{th}C_{th}$ ladder network thermal DPL models, we compare the simulation results with the results obtained from an analytical model of a thermal object with a heat source on the top surface, as shown in Fig. 7.

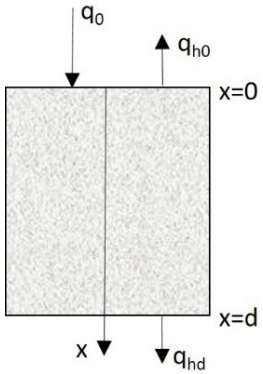


Fig. 7. A porous-like material for modelling heat transfer with the DPL effects

The 1D Fourier–Kirchhoff heat transfer equation for a sourceless sample in the frequency domain can be obtained by applying the Laplace transform for $s = j\omega$, and it takes the form:

$$\frac{\mathrm{d}^2 T}{\mathrm{d}x^2} - \frac{T}{L^2} = 0, \tag{28}$$

where $L$ denotes the diffusion length expressed by (29).

$$L\left(j\omega\right) = \sqrt{\frac{\widetilde{k}}{j\omega c_{th}}}, \tag{29}$$

where $\widetilde{k}$ is the heat conductivity of a material with the DPL effect defined by (1).

The solution of (28) is analytical and takes the form of Eq. (30).

$$T\left(x, j\omega\right) = A\left(j\omega\right) e^{-\frac{x}{L(j\omega)}} + B\left(j\omega\right) e^{\frac{x}{L(j\omega)}}, \tag{30}$$

where $A(j\omega)$ and $B(j\omega)$ are the integration constants.

Let us assume that the sample has a thickness $d$ and is heated by the heat flux $q_0$ at the top surface $x = 0$.

$$-\widetilde{k}\left.\frac{\mathrm{d}T(x)}{\mathrm{d}x}\right|_{x=0} = q_0 - h_0\, T|_{x=0}\,, \tag{31}$$

where $h_0$ is the convective heat transfer coefficient at the top surface.

At the bottom surface, the sample is cooled by convection as well.

$$-\widetilde{k}\left.\frac{\mathrm{d}T(x)}{\mathrm{d}x}\right|_{x=d} = h_d \cdot T\,|_{x=d}\,, \tag{32}$$

where $h_d$ is the heat transfer coefficient at the bottom surface.

Using (31) and (32), it is possible to define the set of 2 linear equations that allow calculating the integration constants $A(j\omega)$ and $B(j\omega)$.

$$\begin{aligned} A\,(j\omega)\left(\frac{\widetilde{k}\,(j\omega)}{L\,(j\omega)} + h_0\right) + B\,(j\omega)\left(-\frac{\widetilde{k}\,(j\omega)}{L\,(j\omega)} + h_0\right) &= q_0, \\ A\,(j\omega)\left(\frac{\widetilde{k}\,(j\omega)}{L\,(j\omega)} - h_d\right) e^{-\frac{d}{L(j\omega)}} + B\,(j\omega)\left(-\frac{\widetilde{k}\,(j\omega)}{L\,(j\omega)} - h_d\right) e^{\frac{d}{L(j\omega)}} &= 0. \end{aligned} \tag{33}$$

The thermal impedance of the sample for the heat source on the upper surface ($x = 0$) takes the form:

$$Z_{th} = \frac{T\,(j\omega)}{P} = \frac{A\,(j\omega) + B\,(j\omega)}{qS}, \tag{34}$$

where $P$ is the Laplace transform of the Dirac function (for $s = j\omega$) with $P = qS$ amplitude, $S$ is the cross-sectional area of the sample from Fig. 7.

## 5. Comparison of analytical and ladder-network modelling results

The analytical model allows one to determine the thermal impedance on the upper surface of the material for $x = 0$ as in Eq. (34). The numerical simulation uses an equivalent thermal ladder electrical network, which essentially means that the Finite Difference Method is used to solve the second-order partial differential equations of heat transfer. This, of course, leads to an approximation of the exact solution.

In order to validate the $R_{th}L_{th}C_{th}$ discrete numerical thermal models of the object with DPL effects of heat transfer, let's consider the n-sectional 1D ladder thermal network presented in Fig. 8. The object is heated up at the top side with power $P$ and cooled down by convection described by the heat transfer coefficients $h_1$ and $h_n$ on both top and bottom sides. In this research, it was assumed that all component thermal impedances and capacitances are equal, $Z_{thi} = Z_{th}$ and $C_{thi} = C_{th}$, for $I = 1, 2, \ldots, n$.

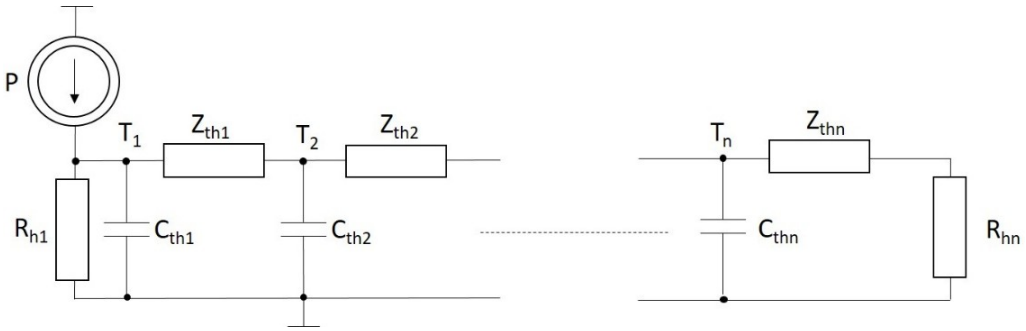


Fig. 8. Thermal ladder model of an object with DPL effects

The impedance $Z_{th}$ depends on the type of model: Fourier–Kirchhoff, SPL, or DPL with excess diffusion or wave propagation in heat transfer.

$$\begin{aligned}
&\text{Fourier–Kirchhoff: } Z_{th} = R_{th},\\
&\text{SPL}\left(\tau_q = 0\right) : Y_{th} = G_{th}\left(1 + j\omega\tau_T\right),\\
&\text{SPL}\left(\tau_T = 0\right) : Z_{th} = R_{th}\left(1 + j\omega\tau_q\right),\\
&\text{DPL}\left(\tau_T > \tau_q\right) : Y_{th} = G_{th}\left(1 + \frac{1}{\frac{1}{j\omega\Delta\tau} + \frac{\tau_q}{\Delta\tau}}\right),\\
&\text{DPL}\left(\tau_q > \tau_T\right) : Z_{th} = R_{th}\left(1 + \frac{1}{\frac{1}{j\omega\Delta\tau} + \frac{\tau_T}{\Delta\tau}}\right),
\end{aligned} \tag{35}$$

where $R_{th}$ is defined by (9), $G_{th} = 1/Z_{th}$ and $\Delta\tau = |\tau_T - \tau_q|$.

The comparison results of the modelling are presented qualitatively in the figures below and quantitatively using the mean relative error defined by:

$$\text{err} = \frac{1}{N}\sum_{i=1}^{N}\left|\frac{Z_{th}\left(\omega_i\right) - \widetilde{Z}_{th}\left(\omega_i\right)}{Z_{th}\left(\omega_i\right)}\right|, \tag{36}$$

where $Z_{th}$ and $\widetilde{Z}_{th}$ denote the impedances obtained from the analytical and ladder $R_{th}L_{th}C_{th}$ models, and $N$ is the number of frequency points in the simulations.

All presented simulation results were performed for a porous-like material filled with water, comparable to tissue. The values of the parameters presented in Table 1 are the same in analytical and numerical models.

All simulation results are obtained for $\omega\epsilon(10^{-7}, 1)$ 1/s and the number of nodes in the ladder $M = 1\,000$. Figure 9 presents the comparative results for classical Fourier–Kirchhoff's models. As can be noticed, the discrepancy is seen in the high-frequency range. Relative mean error does not exceed 1%. The dashed line shows the $-\pi/4$ asymptote for which the Nyquist plot converges at high frequencies for a sample of semi-infinity or of sufficient length.

Table 1. Values of parameters used in modelling

| Parameter | Value | Unit |
|---|---|---|
| $k$ | 1.5 | W/mK |
| $c_{th}$ | 3 900 000 | J/m$^3$K |
| $h_n$ | 10 | W/m$^2$K |
| $h_d$ | 10 | W/m$^2$K |
| $d$ | 0.1 | m |
| $S$ | $0.05 \times 0.05$ | m$^2$ |
| $q_0$ | 100 | W/m$^2$ |
| $\omega_{\min} - \omega_{\max}$ | $10^{-7} - 1$ | 1/s |
| Number of nodes | 1 000 | – |

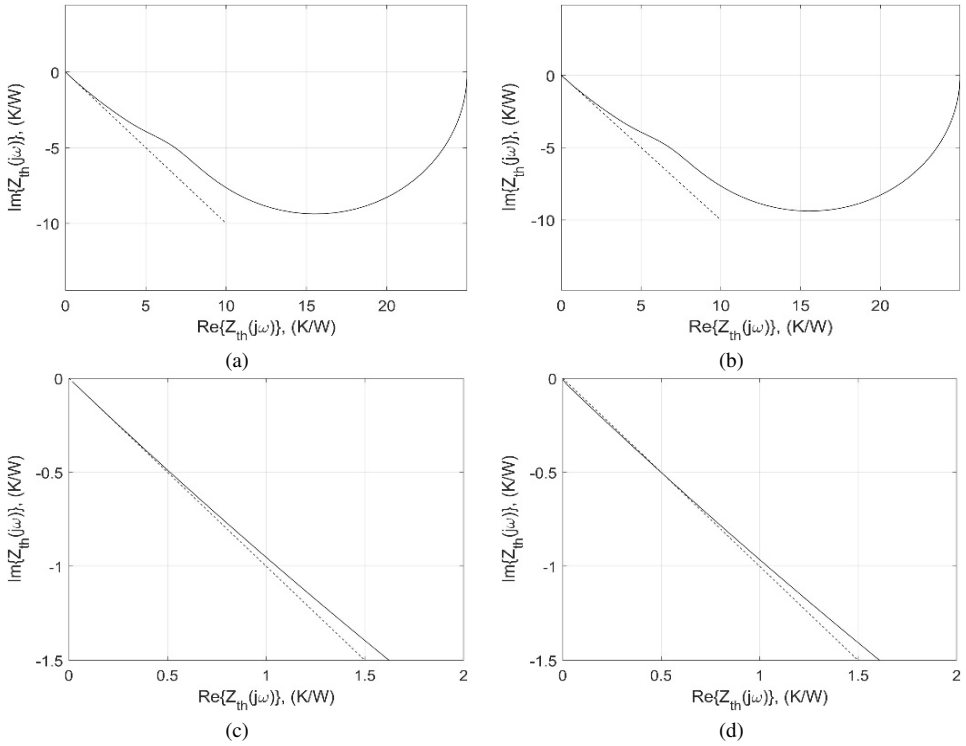


Fig. 9. Results comparison of analytical (a) and $R_{th}C_{th}$ ladder Fourier–Kirchhoff's model (b) – $\tau_T = 0$ s, $\tau_q = 0$ s, err = 0.99%. Subfigures (c) and (d) show a zoomed view of a higher range of frequencies, respectively

Figure 10 presents the comparative results for SPL models with purely diffusive heat transfer ($\tau_T = 10$ s, $\tau_q = 0$ s). In this case, the relative mean error is lower compared to the F–K models and is equal to 0.65%.

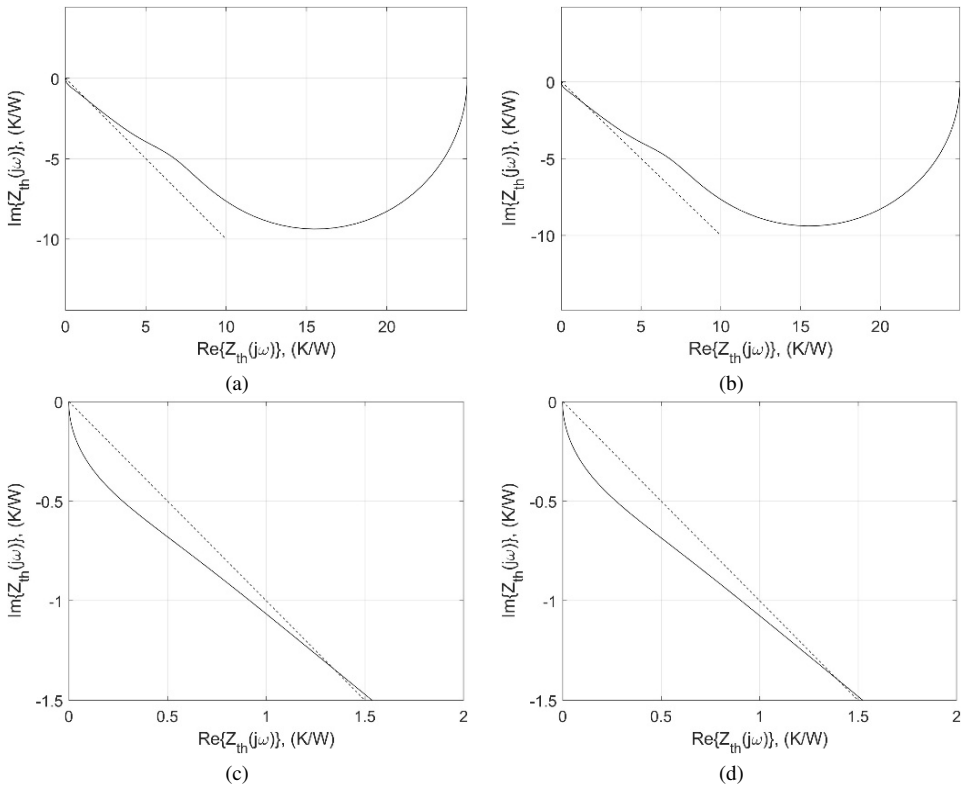


Fig. 10. Results comparison of analytical (a) and $R_{th}C_{th}$ ladder SPL model (b) – $\tau_T = 10$ s, $\tau_q = 0$ s, err = 0.65%. Subfigures (c) and (d) show a zoomed view of a higher range of frequencies, respectively

Figure 11 presents the comparative results for DPL models with excess diffusive heat transfer ($\tau_T = 10$ s, $\tau_q = 2$ s). In this case, the relative mean error is lower compared to the F–K model and is equal to 0.7%.

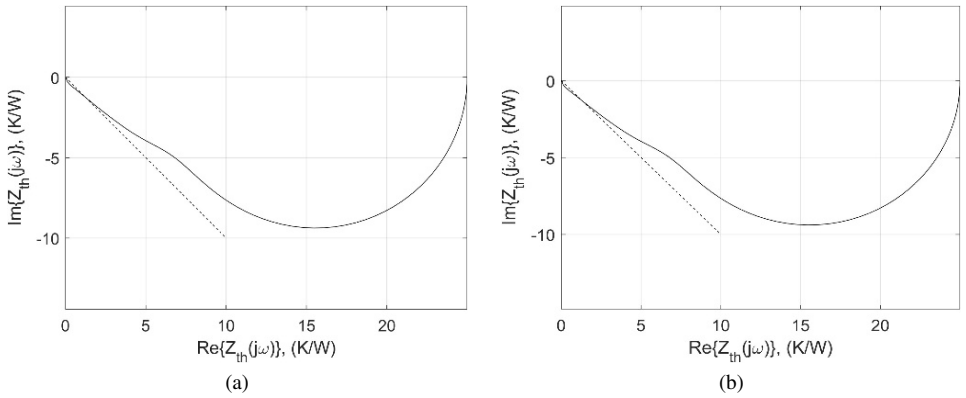

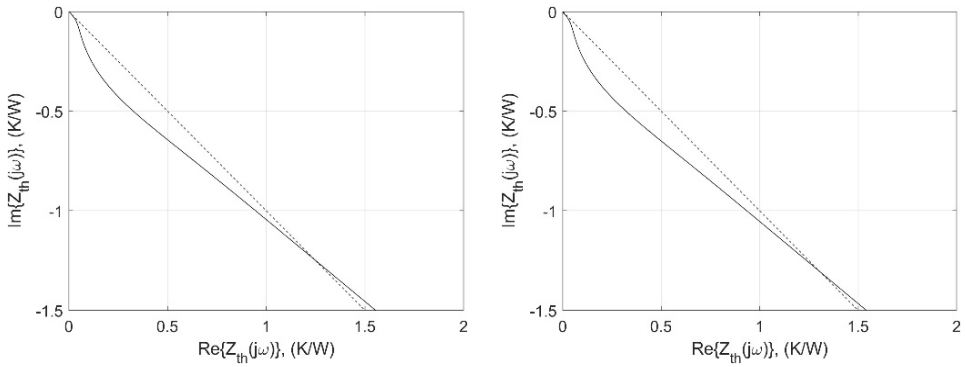


Fig. 11. Results comparison of analytical (a) and $R_{th}C_{th}$ ladder DPL diffusive propagation model (b) – $\tau_T = 10$ s, $\tau_q = 2$ s, err = 0.7%. Subfigures (c) and (d) show a zoomed view of a higher range of frequencies, respectively

Interesting results can be obtained for the SPL model with purely wave propagation heat transfer ($\tau_T = 0$ s, $\tau_q = 10$ s) in the frequency range $\omega\epsilon(10^{-7}, 1)$ 1/s. The simulation results show the discrepancy in the high-frequency range, as shown in Fig. 12. The analytical model displays the asymptotic approach of $Z_{th}$ curve to the point of pure resistive character. The $Z_{th}$ characteristic of the ladder numerical model shows convergence at $Z_{th} \to 0$. Moreover, in this case, a non-monotonic convergence can be observed with a kink in the curve near the resonant frequency, which depends on the model parameters, e.g.: $\tau_q$, $L_{thq}$ and $C_{th}$. As a result, the relative mean error increases to 1.8%.

The results of Fig. 12 need further clarification. The analytical solution converges to a constant and pure resistive value. Also, the results obtained with the ladder network show something similar. At first, the impedance also seems to converge to a constant resistive value, but finally it tends to zero. These results are well known in the domain of electromagnetic radiation and transmission line theories. At high frequencies (Fig. 12), the impedance of the inductor $|\omega L_{thq}|$ is so high that the series resistance $R_{th}$ turns out to be negligible. What remains is a classical $LC$ transmission line. In many textbooks, it has been proved that an infinitely long transmission line behaves like a resistor $R_0$ and its value is given by:

$$R_0 = \sqrt{\frac{L_{thq}}{C_{th}}}, \tag{37}$$

where

$$L_{thq} = \tau_q R_{th} = \tau_q \frac{\Delta x}{kS} \tag{38}$$

and

$$C_{th} = c_{th} S \Delta x. \tag{39}$$

By inserting the numerical values listed in Table 1, we get $R_0 = 0.5225 \ \frac{\mathrm{K}}{\mathrm{W}}$, which agrees perfectly with the plot shown in Fig. 12.

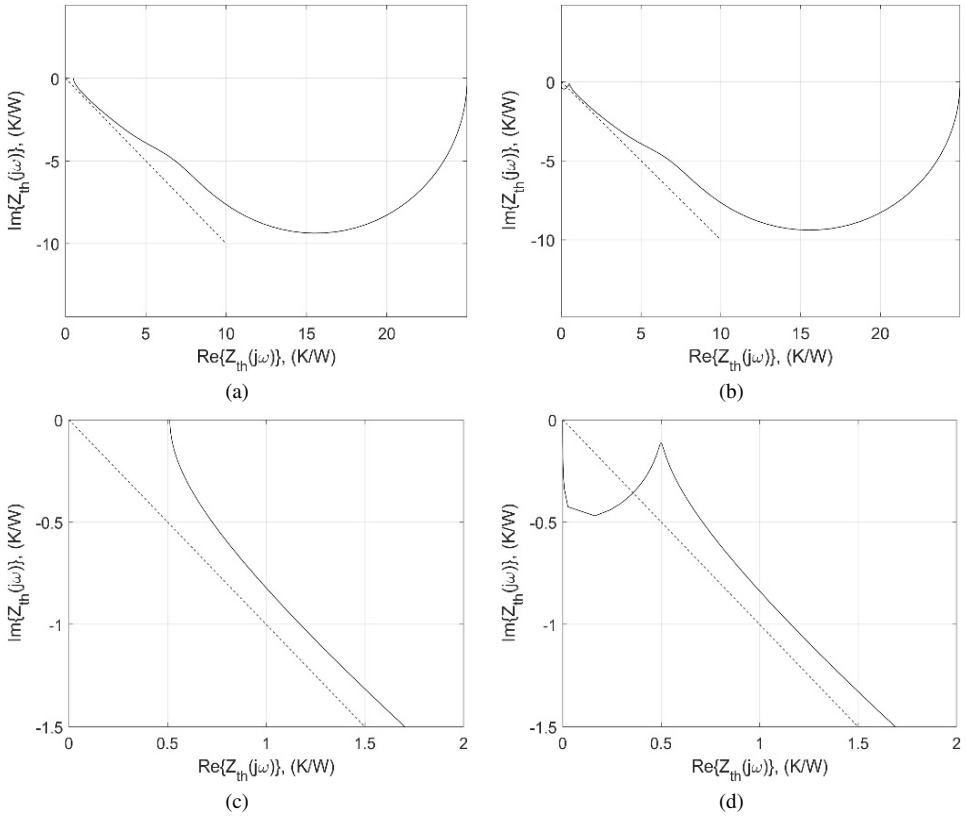


Fig. 12. Results comparison of analytical (a) and $R_{th}C_{th}$ ladder DPL wave model (b) – $\tau_T = 0$ s, $\tau_q = 10$ s, err = 1.8%. Subfigures (c) and (d) show a zoomed view of a higher range of frequencies, respectively

For the sake of completeness, one can also get the propagation velocity $v$ of the thermal wave:

$$v = \frac{\Delta x}{2\pi\sqrt{L_{thq}C_{th}}} = \frac{1}{2\pi}\sqrt{\frac{k}{\tau_q c_{th}}} = 0.0312 \text{ mm/s}. \tag{40}$$

Note that to obtain $v$, we have to use the inductance and the capacitance per unit length. The speed value is very low due to the value $\tau_q = 10$ s. For values of $\tau_q$ in the picosecond range, propagation speeds approaching the speed of sound can be obtained.

The final simulation was performed for DPL models with mixed wave propagation and diffusive heat transfer for $\tau_T = 2$ s, $\tau_q = 10$ s. The results show the greatest discrepancy in the high frequency range with the relative mean error reaching as much as 5.92% as shown in Fig. 13.

In order to improve the simulation accuracy in the high-frequency range, it is recommended to decrease the distance step $\Delta x$ in numerical modelling. Unfortunately, this significantly increases the number of nodes and simulation time. This problem is discussed in the next section.

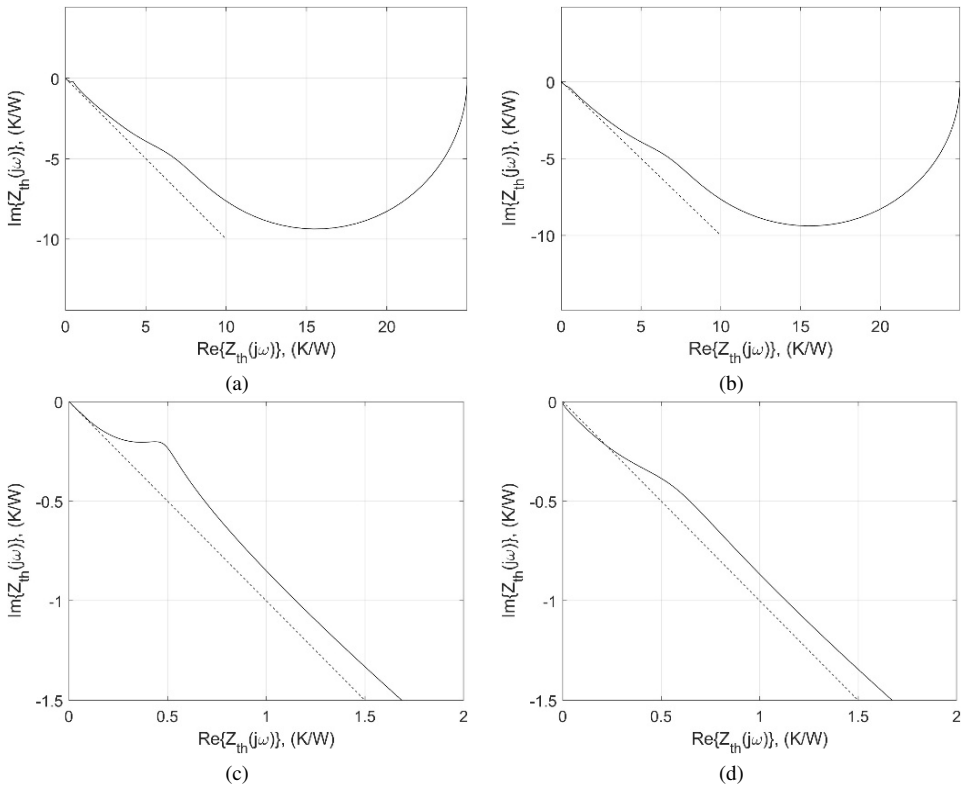


Fig. 13. Results comparison of analytical (a) and $R_{th}C_{th}$ ladder DPL diffusive model (b) – $\tau_T = 2$ s, $\tau_q = 10$ s, err = 5.92%. Subfigures (c) and (d) show a zoomed view of a higher range of frequencies, respectively

## 6. Discussion

In order to select the optimum number of sections in the $R_{th}L_{th}C_{th}$ ladder network, it's worth noting that the electrical analogy of heat conduction is based on the FDM and the Taylor expansion of temperature. For solving the 1D heat transfer equation, the second derivative with respect to $x$ is approximated by:

$$\frac{\partial^2 T}{\partial x^2} = T^{(2)}(x) \approx \frac{T_{i+1} - 2T_i + T_{i-1}}{\Delta x^2} = \widetilde{T}^{(2)}(x), \tag{41}$$

where $T^{(2)}(x)$ and $\widetilde{T}^{(2)}(x)$ denote the second-order derivative of temperature with respect to $x$ and its FDM approximation, respectively.

Using the Taylor theorem for $T(x + \Delta x)$ and $T(x - \Delta x)$, it is possible to represent the second derivative of temperature as:

$$T^{(2)}(x) = \widetilde{T}^{(2)}(x) + R(\Delta x), \tag{42}$$

where the reminder $(R\Delta x)$ takes the form:

$$R\left(\Delta x\right) = -\frac{2T^{(4)}\left(x\right)}{4!}\Delta x^2 - \frac{2T^{(6)}\left(x\right)}{6!}\Delta x^4 - \ldots = \sum_{i=2}^{\infty}\frac{2T^{(2i)}\left(x\right)}{(2i)!}\Delta x^{2(i-1)}. \tag{43}$$

The reminder $R$ is not only a function of $x$ but also of $\omega$ and must be taken as a small enough value to provide an acceptable approximation. It allows one to estimate the distance step $\Delta x$ of the FDM approximation, which is strongly correlated with the maximum angular frequency of the analysis in the frequency domain.

$$\left|R\left(\Delta x, \omega\right)\right| < \epsilon. \tag{44}$$

If we limit this approximation analysis to the first element of the series (43) and take the analytical solution of the heat transfer model (30) to obtain the fourth-order derivative of temperature, the approximation error $R(h, \omega)$ can be expressed as:

$$\frac{2}{(4!)}\left|\frac{A(j\omega) + B(j\omega)}{L^4(j\omega)}\right|\Delta x^2 < \epsilon. \tag{45}$$

Assuming a given approximation error $\epsilon$ and using (29), the distance step $\Delta x$ with respect to $\omega$ can be estimated as:

$$\Delta x = \sqrt{12\epsilon}\left|\frac{\widetilde{k}(j\omega)}{j\omega c_{th}\sqrt{A(j\omega) + B(j\omega)}}\right| = \sqrt{12\epsilon}\left|\frac{\widetilde{k}(j\omega)}{j\omega c_{th}\sqrt{T(j\omega)|_{x=0}}}\right|. \tag{46}$$

The results of the accuracy analysis for 2 given frequencies are presented in Table 2. They confirm the strong dependence between the distance step $\Delta x$ and the maximum angular frequency used for modelling.

Table 2. Distance step $\Delta x$ for maximum angular frequencies $\omega_{\max} = 1$ and 0.1 1/s, $\epsilon = 10^{-4}$ K/m$^2$

| **Model** | **$\omega_{\max}$, 1/s** | **Distance step $\Delta x$, m** |
|---|---|---|
| Fourier–Kirchhoff | 1 | $6.487 \times 10^{-8}$ |
| | 0.1 | $3.659 \times 10^{-7}$ |
| SPL, $\tau_T = 10$ s | 1 | $1.159 \times 10^{-6}$ |
| | 0.1 | $5.629 \times 10^{-7}$ |
| DPL, $\tau_T = 10$ s, $\tau_q = 2$ s | 1 | $4.241 \times 10^{-7}$ |
| | 0.1 | $5.496 \times 10^{-7}$ |
| SPL, $\tau_q = 10$ s | 1 | $3.644 \times 10^{-9}$ |
| | 0.1 | $2.378 \times 10^{-7}$ |
| DPL, $\tau_q = 10$ s, $\tau_T = 2$ s | 1 | $9.934 \times 10^{-9}$ |
| | 0.1 | $2.436 \times 10^{-7}$ |

It is worth emphasizing that the distance step $\Delta x$ decreases with the square root of the error $\sqrt{\epsilon}$. At the same time, this step increases with the maximum frequency of thermal analysis. To ensure high modeling accuracy, the $\epsilon$ error must be kept at a sufficiently low level, which significantly increases the number of nodes in the $R_{th}L_{th}C_{th}$ ladder and consequently increases the analysis time.

The thermal modelling results presented in this paper refer to the frequency domain. Such an approach significantly reduces the calculations and, in some cases, makes them analytical, in particular in the case of one-dimensional Kirchhoff–Fourier and DPL modelling of single- and multilayer thermal structures. Consequently, it allows for deeper insight into the thermal phenomena under consideration and a more reliable interpretation of the obtained results. In bioengineering, when distinguishing between pathological and physiological cases, it is easier to make such a diagnosis because some anomalous temperature changes may be more pronounced in the frequency domain. The integral Fourier or Laplace transforms used in this analysis significantly reduce the ubiquitous noise in the measurements, especially in the case of weak temperature changes detected by non-contact measurement systems. Currently, sub-noise temperature measurements are possible using high-speed thermal imaging cameras [46]. In electronics and electrical engineering, analysis of temperature frequency spectra allows for the explanation of thermal phenomena occurring at different frequencies, which can sometimes be unexpected. For example, high-frequency temperature components become independent of ambient cooling conditions, unlike mean temperature and slow temperature changes. As a result, frequency analysis can be used to precisely characterize the electrical state of the measurement system [47]. Moreover, temperature frequency analysis directly corresponds to the commonly used thermal characterization of power electronics using thermal time constant spectra [48, 49]. It is worth noting that frequency analysis does not eliminate the possibility of presenting temperature evolution in the time domain, and in some cases, it even makes it easier. There are many numerical methods for converting frequency spectra into time-dependent signals. These include the inverse Fourier and Laplace transforms, the Vector Fitting method, Continuous-time System Identification (CONTSID) [50, 51], the Computer-Aided Program for Time-series Analysis and Identification of Noisy Systems (CAPTAIN) [52], and Transfer Function Estimation (TFEST) [53, 54].

## 7. Conclusions

Due to the progress and wide application of nanotechnology, smart and composite materials, and multi-phase thin-film structures, non-Fourier heat transfer modelling is becoming more and more attractive and necessary for use. Such modelling has already been implemented in many simulation tools, used mainly for research and prototyping. In many cases, this requires powerful computer tools equipped with additional units that increase speed and available memory, and finally, the FEM simulation environment must be installed. In many cases, such simulations, especially for 3-dimensions, take hours.

For engineering applications, it is more helpful to use simulation tools that are not as advanced but provide satisfactory results in a short time, almost immediately. This gives the possibility of performing iterative analysis by frequently adjusting key parameters, e.g. to match simulation and measurement results during prototyping. For these applications the compact and the ladder simplified thermal modelling has been developed. It is worth underlining that the ladder models

presented in this research can be easily extended to multilayer structures. In addition, comparing to the compact modelling, the ladders can model 2D and 3D geometrically complex thermal structures, and definitely they do not need high computer power.

The modelling presented above is based on the concept of temperature and heat flux delays. There has been a scientific discussion on the thermodynamic consistency of this approach, especially for the wave propagation mode of heat transfer in very thin materials excited by very short energy pulses. Among others, for these applications, a compact and simplified ladder thermal modelling has been developed. It is worth emphasizing that the ladder models presented in this study can be easily extended to multilayer structures. Moreover, similarly to compact modelling, ladders can model 2D and 3D geometrically complex thermal structures and definitely do not need high computational power. It seems that the thermal ladder approximation in single and double-phase delay modelling could contribute to the validation of non-Fourier heat transfer and help in the interpretation of the obtained results, as well as simplify calculations. Such modelling can be useful in a variety of applications, including thermal and electrical engineering.

**Acknowledgments**

The research presented in this paper was financed by the National Science Centre, project OPUS23 no. 2022/45/B/ST7/02820.

**References**

[1] Tzou D.Y., *Macro-to Microscale Heat Transfer: The Lagging Behavior*, 2nd ed., Wiley (2014), DOI: 10.1002/9781118818275.

[2] Askarizadeh H., Ahmadikia H., *Extended Irreversible Thermodynamics Versus Second Law Analysis of High-Order Dual-Phase-Lag Heat Transfer*, ASME Journal of Heat and Mass Transfer, vol. 140, 082003 (2018), DOI: 10.1115/1.4038851.

[3] Rukolaine S.A., *Unphysical effects of the dual-phase-lag model of heat conduction: higher-order approximations*, International Journal of Thermal Sciences, vol. 113, pp. 83–88 (2017), DOI: 10.1016/j.ijthermalsci.2016.11.016.

[4] Cattaneo C., *A form of heat conduction equation which eliminates the paradox of instantaneous propagation*, Comptes Rendus, vol. 247, pp. 431–433 (1958), DOI: ci.nii.ac.jp/naid/10018112216.

[5] Vernotte P., *Les paradoxes de la theorie continue de l'equation de la chaleur*, Comptes Rendus, vol. 246, pp. 3154–3155 (1958).

[6] Mochnacki B., Paruch M., *Cattaneo-Vernotte Equation. Identification of Relaxation Time Using Evolutionary Algorithms*, Journal of Applied Mathematics and Computational Mechanics, vol. 12, pp. 97–102 (2013).

[7] Majchrzak E., *Modeling of skin tissue heating using the generalized dual phase-lag equation*, Archives of Mechanics, vol. 67, pp. 417–437 (2015).

[8] Zhang Y., *Generalized dual-phase lag bioheat equations based on nonequilibrium heat transfer in living biological tissues*, International Journal of Heat and Mass Transfer, vol. 52, pp. 4829−4834 (2009), DOI: 10.1016/j.ijheatmasstransfer.2009.06.007.

[9] Kumar R., Vashishth A.K., Ghangas S., *Phase-Lag Effects in Skin Tissue during Transient Heating*, International Journal of Applied Mechanics and Engineering, vol. 24, pp. 603–623 (2019), DOI: 10.2478/ijame-2019-0038.

[10] Sharma S.K., Kumar D., *A Study on Non-Linear DPL Model for Describing Heat Transfer in Skin Tissue during Hyperthermia Treatment*, Entropy, vol. 22, 481 (2020), DOI: 10.3390/e22040481.

[11] Kumar D., Singh S., Sharma N., Rai K.N., *Verified non-linear DPL model with experimental data for analyzing heat transfer in tissue during thermal therapy*, International Journal of Thermal Sciences, vol. 133, pp. 320–329 (2018), DOI: 10.1016/j.ijthermalsci.2018.07.031.

[12] Zhmakin A.I., *The Zoo of Non-Fourier Heat Conduction Models*, arXiv preprint arXiv:2212.12922 (2022), DOI: 10.48550/arXiv.2212.12922.

[13] Nie B.-D., Cao B.-Y., *Three mathematical representations and an improved ADI method for hyperbolic heat conduction*, International Journal of Heat and Mass Transfer, vol. 135, pp. 974−984 (2019), DOI: 10.1016/j.ijheatmasstransfer.2019.02.026.

[14] Chen G., *Non-Fourier phonon heat conduction at the microscale and nanoscale*, Nature Reviews Physics, vol. 3, pp. 555–569 (2021), DOI: 10.1038/s42254-021-00334-1.

[15] Wang M., Yang N., Guo Z.Y., *Non-Fourier heat conductions in nanomaterials*, Journal of Applied Physics, vol. 110, 064310 (2011), DOI: 10.1063/1.3634078.

[16] Nakayama A., Kuwahara F., *A general bioheat transfer model based on the theory of porous media*, International Journal of Heat and Mass Transfer, vol. 51, pp. 3190–3199 (2008), DOI: 10.1016/j.ijheatmasstransfer.2007.05.030.

[17] Sahoo N., Ghosh S., Narasimhan A., Das S.K., *Investigation of non-Fourier effects in bio-tissues during laser-assisted photothermal therapy*, International Journal of Thermal Sciences, vol. 76, pp. 208–220 (2014), DOI: 10.1016/j.ijthermalsci.2013.08.014.

[18] Tzou D.Y., *Lagging behavior in biological systems*, Journal of Heat Transfer, vol. 134, 051006 (2012), DOI: 10.1115/1.4005636.

[19] Li X., Li Y., Luo P., Tian X., *Relationship between the nonlocal effect and lagging behavior in bioheat transfer*, Journal of Heat Transfer, vol. 143, 051201 (2021), DOI: 10.1115/1.4049997.

[20] Liu K.C., Yang Y.C., *Numerical analysis of local nonequilibrium heat transfer in layered spherical tissue during magnetic hyperthermia*, Computer Methods in Biomechanics and Biomedical Engineering, pp. 1–13 (2020), DOI: 10.1080/10255842.2020.1779232.

[21] Saeed T., Abbas I., *Finite element analyses of nonlinear DPL bioheat model in spherical tissues using experimental data*, 15th Quantitative InfraRed Thermography Conference, Porto, Portugal (2020), DOI: 10.1080/15397734.2020.1749068.

[22] Chaudhary R.K., Kumar D., Rai K.N., Singh J., *Numerical simulation of the skin tissue subjected to hyperthermia treatment using a nonlinear DPL model*, Thermal Science and Engineering Progress, vol. 34, 101394 (2022), DOI: 10.1016/j.tsep.2022.101394.

[23] Strąkowska M., Więcek B., De Mey G., *Comparison of the Fourier–Kirchhoff, Pennes and DPL thermal models of a single layer tissue*, 15th Quantitative InfraRed Thermography Conference (2020), DOI: 10.21611/qirt.2020.127.

[24] Strąkowska M., De Mey G., Więcek B., *Experimental verification of non-Fourier heat transfer in a multilayer skin tissue structure by IR temperature measurement*, 16th Quantitative InfraRed Thermography Conference, Paris, France (2022), DOI: 10.21611/qirt.2022.1023.

[25] Strąkowska M., De Mey G., Więcek B., *Identification of the Thermal Constants of the DPL Heat Transfer Model of a Single Layer Porous Material*, Pomiary Automatyka Robotyka, vol. 2, pp. 41–46 (2021), DOI: 10.14313/PAR_240/41.

[26] Strąkowska M., De Mey G., Więcek B., *DPL Non-Fourier Heat Transfer Modelling in Porous Materials and Validation using IR Measurement*, Proceedings of the 17th Quantitative InfraRed Thermography Conference (QIRT 2024), Zagreb, Croatia (2024).

[27] Ordonez-Miranda J., Alvarado-Gil J.J., *On the Stability of the Exact Solutions of the Dual-Phase Lagging Model of Heat Conduction*, Nanoscale Research Letters, vol. 6, 327 (2011), DOI: 10.1186/1556-276X-6-327.

[28] Kovács R., Ván P., *Thermodynamical consistency of the dual-phase-lag heat conduction equation*, Continuum Mechanics and Thermodynamics, vol. 30, pp. 1223–1230 (2018), DOI: 10.48550/arXiv.1709.06825.

[29] Liu K.-C., Chen H.-T., *Investigation for the dual phase lag behavior of bio-heat transfer*, International Journal of Thermal Sciences, vol. 49, pp. 1138–1146 (2010), DOI: 10.1016/j.ijthermalsci.2010.02.007.

[30] Zubert M., Raszkowski T., Samson A., Zając P., *Methodology of determining the applicability range of the DPL model to heat transfer in modern integrated circuits comprised of FinFETs*, Microelectronics Reliability, vol. 91, pp. 139–153 (2018), DOI: 10.1016/j.microrel.2018.07.141.

[31] Youssef H.M., Alghamdi N.A., *The exact analytical solution of the dual-phase-lag two-temperature bioheat transfer of a skin tissue subjected to constant heat flux*, Scientific Reports, vol. 10, 15946 (2020), DOI: 10.1038/s41598-020-73086-0.

[32] Xu M., *Thermodynamic basis of dual-phase-lagging of heat conduction*, Journal of Heat Transfer, vol. 133, 041401 (2011), DOI: 10.1115/1.4002983.

[33] Górecki K., Zarębski J., Górecki P., Ptak P., *Compact Thermal Models of Semiconductor Devices: A Review*, International Journal of Electronics and Telecommunications, vol. 65, pp. 151–158 (2019), DOI: 10.24425/ijet.2019.126295.

[34] Azizian D., Bigdelia M., *A new cast-resin transformer thermal model based on recurrent neural networks*, Archives of Electrical Engineering, vol. 66, no. 1, pp. 17–28 (2017), DOI: 10.1515/aee-2017-0002.

[35] Du M., Guo Q., Wang H., Ouyang Z., Wei K., *An Improved Cauer Model of IGBT Module: Inclusive Void Fraction in Solder Layer*, IEEE Transactions on Components, Packaging and Manufacturing Technology, vol. 10, pp. 1401–1410 (2020), DOI: 10.1109/TCPMT.2020.3010064.

[36] Liu X., Grassi F., Spadacini G., Pignari S.A., Trotti F., Mora N., Hirschi W., *Behavioral Modeling of Complex Magnetic Permeability with High-Order Debye Model and Equivalent Circuits*, IEEE Transactions on Electromagnetic Compatibility, vol. 63, pp. 730–738 (2021), DOI: 10.1109/TEMC.2020.3016376.

[37] Sato Y., Kawano K., Igarashi H., Matsumoto H., *Extended Cauer Equivalent Circuit Model of Inductors: Representing Multi-resonant Characteristics Due to Parasitic Capacitance*, 2023 IEEE Applied Power Electronics Conference and Exposition (APEC), pp. 3294–3301 (2023), DOI: 10.1109/APEC43580.2023.10131598.

[38] Jabłoński M., De Mey G., Kos A., *Quad configuration for improved thermal design of cascade current mirror*, Electronics Letters, vol. 48, pp. 80–82 (2012), DOI: 10.1049/el.2011.2955.

[39] Górecki K., Ptak P., *Simple Form of Compact Thermal Model of the Large LED Modules*, Energies, vol. 16, 7329 (2023), DOI: 10.3390/en16217329.

[40] JEDEC Standard JESD15-4, *DELPHI Compact Thermal Model Guideline, Solid State Technology Association* (2008).

[41] Siemens Digital Industries Software, *Embeddable BCI-ROM Technology: Reduced Order Thermal Models for 3D CFD Electronics Cooling Simulation* (2024), available at: https://blogs.sw.siemens.com/simcenter/embeddable-bci-rom-cfd-thermal-model/, accessed July 2025.

[42] Ansys Icepak User's Guide, *Icepak 2024 R2 Documentation* (2024), available at: https://ansyshelp.ansys.com/public/account/secured?returnurl$=$///Views/Secured/corp/v242/en/ice_ug/ice_ug.html, accessed July 2025.

[43] Zeinali B., Mojra A., Vafai K., *Analysis of HIFU thermal ablation for lung cancer incorporating local thermal non-equilibrium and non-Fourier transfer*, International Communications in Heat and Mass Transfer, vol. 159, part C, 108273 (2024), DOI: 10.1016/j.icheatmasstransfer.2024.108273.

[44] Al-Masri A., *Thermal modeling of porous medium integrated in PCM and its application in passive thermal management of electric vehicle battery pack*, Journal of Applied Physics, vol. 136, no. 3, 035001 (2024), DOI: 10.1063/5.0221003.

[45] Olbrycht R., Kałuża M., Felczak M., Levchenko D., Więcek B., *Potential of Indirect Regenerative Evaporative Cooling System (M-Cycle) for Electronic Applications*, Pomiary Automatyka Robotyka, vol. 27, no. 3, pp. 19–25 (2023), DOI: 10.14313/PAR_249/19.

[46] Strąkowska M., De Mey G., Więcek B., *Non-Fourier heat transfer in porous material with experiment using periodic power excitations and IR thermography*, Quantitative InfraRed Thermography Journal, pp. 1–16 (2025), DOI: 10.1080/17686733.2025.2572872.

[47] Torzyk B., Więcek B., *Second-harmonic contactless method for measurement of RMS current using a standard infrared camera*, IEEE Transactions on Instrumentation and Measurement, vol. 70, no. 2004308, pp. 1–8 (2021), DOI: 10.1109/TIM.2021.3077676.

[48] Szekely V., *On the representation of infinite-length distributed RC one-ports*, IEEE Transactions on Circuits and Systems, vol. 38, no. 7, pp. 711–719 (1991), DOI: 10.1109/31.135743.

[49] Szekely V., *Identification of RC networks by deconvolution: chances and limits*, IEEE Transactions on Circuits and Systems I: Fundamental Theory and Applications, vol. 45, no. 3, pp. 244–258 (1998), DOI: 10.1109/81.662698.

[50] Garnier H., Mensler M., Richard A., *Continuous-time model identification from sampled data: implementation issues and performance evaluation*, Journal of Control, vol. 76, no. 13, pp. 1337–1357 (2003), DOI: 10.1080/0020717031000149636.

[51] Ljung L., *Experiments with identification of continuous-time models*, IFAC Proceedings Volumes, vol. 42, no. 10, pp. 1175–1180 (2009), DOI: 10.3182/20090706-3-FR-2004.00195.

[52] *CAPTAIN – Computer-Aided Program for Time-Series Analysis and Identification of Noisy Systems*, available at: http://www.es.lancs.ac.uk/cres/captain/, accessed October 2025.

[53] Strąkowska M., Chatzipanagiotou P., De Mey G., Chatziathanasiou V., Więcek B., *Multilayer thermal object identification in frequency domain using IR thermography and vector fitting*, International Journal of Circuit Theory and Applications, vol. 48, pp. 1523–1533 (2020), DOI: 10.1002/cta.2845.

[54] Ozdemir A.A., Gumussoy S., *Transfer Function Estimation in System Identification Toolbox via Vector Fitting*, IFAC-PapersOnLine, vol. 50, no. 1, pp. 6232–6237 (2017), DOI: 10.1016/j.ifacol.2017.08.1026.